Nano Research

Open Access

Research Article

Adipose-targeted microneedle patch co-delivering semaglutide and rosiglitazone unlocks adipose browning efficacy for obesity therapy

Weiqin Yao[§], Jiawen Wang[§], Xuan Zeng ✉, Weihai Chen ✉, and Xianzheng Zhang ✉

Key Laboratory of Biomedical Polymers of Ministry of Education & Department of Chemistry, Wuhan University, Wuhan 430072, China
§ Weiqin Yao and Jiawen Wang contributed equally to this work.

Cite this article: *Nano Research*, **2026**, *19*, 94908852. https://doi.org/10.26599/NR.2026.94908852

ABSTRACT: Current clinical management of obesity relies primarily on glucagon-like peptide-1 (GLP-1) receptor agonists or peroxisome proliferator-activated receptor gamma (PPAR-γ) agonists. However, GLP-1 agonists often lead to weight regain after discontinuation, while PPAR-γ agonist efficacy is limited by the pro-inflammatory adipose microenvironment. Here, we report an adipose-targeted nanocomposite microneedle patch (LRSG-SG@MN) for obesity treatment via an immuno-metabolic modulation strategy based on the co-delivery of rosiglitazone and semaglutide. This platform leverages the intrinsic affinity of nano-lipid droplets for adipocytes to deliver rosiglitazone, thereby activating PPAR-γ signaling and initiating mitochondrial biogenesis. Concurrently, the sustained release of semaglutide reprograms the local immune microenvironment by driving macrophage polarization from pro-inflammatory M1 to anti-inflammatory M2 phenotypes. Mechanistically, this resolution of adipose inflammation alleviates the suppression of thermogenesis, creating a circuit that potentiates the browning effects of rosiglitazone. In high-fat diet-induced obese mice, this strategy demonstrated robust efficacy, significantly reducing adiposity and ameliorating glucolipid metabolic disorders. Notably, the system exhibited excellent weight maintenance capacity following treatment cessation without significant rebound, achieving efficient and durable anti-obesity outcomes. This study unveils the non-central immunomodulatory function of semaglutide and establishes an adipose-targeted, long-acting nanocomposite microneedle platform that achieves combined therapeutic outcomes through adipose tissue inflammatory reprogramming coupled with browning induction, offering a novel strategy for sustainable obesity management.

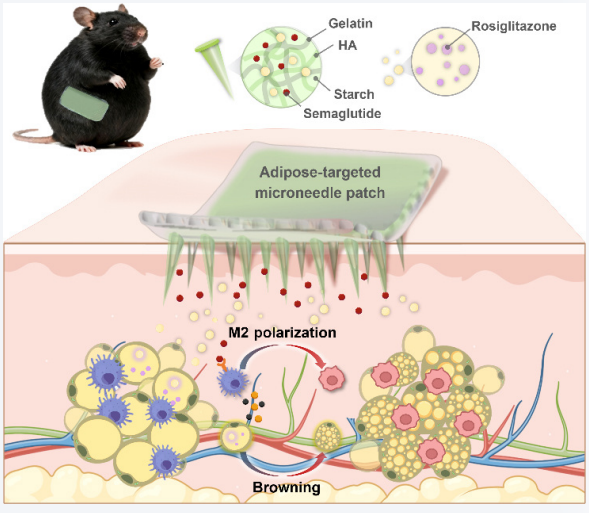

KEYWORDS: nanomedicine, obesity therapy, inflammation regulation, adipocyte browning, microneedle patch

1 Introduction

The global obesity pandemic represents one of the most pressing public health challenges of the twenty-first century [1–3]. As of 2025, more than 3 billion individuals meet criteria for obesity [4–7]. Projections from the World Obesity Atlas suggest that this figure will exceed 4 billion by 2035, surpassing 51% of the global population [8–10]. This trajectory positions obesity as the predominant non-communicable disease burden worldwide. Obesity drives chronic inflammation in visceral adipose tissue, substantially elevating the risk of cardiovascular diseases, Type II diabetes, metabolic dysfunction-associated steatotic liver disease (MASLD), and malignancy [11–14].

Semaglutide, a first-in-class glucagon-like peptide-1 (GLP-1) receptor agonist currently approved for obesity management, achieves its anorexigenic and weight-reducing effects predominantly via central GLP-1 receptor activation on hypothalamic arcuate nucleus neurons, thereby modulating energy homeostasis via appetite suppression [15–18]. Notwithstanding its robust efficacy, this neurocentric mechanism precipitates profound weight recidivism following treatment discontinuation, posing a

Received: March 28, 2026; **Revised:** May 15, 2026
Accepted: May 18, 2026

✉Address correspondence to Xuan Zeng, xuanzeng@whu.edu.cn; Weihai Chen, chenweihai@whu.edu.cn; Xianzheng Zhang, xzzhang@whu.edu.cn

fundamental barrier to sustainable metabolic improvement [19–21]. To circumvent this limitation, prior investigative efforts have explored the adjunctive deployment of adipose-targeted browning agents to augment energy expenditure by enhancing brown adipose tissue activity [22–24]. However, the efficacy of this approach is markedly attenuated by the chronically inflamed state of adipose tissue in obesity, wherein pro-inflammatory cytokine networks antagonize thermogenic gene expression programs [25–27]. Thus, the development of integrated therapeutic strategies that simultaneously address the transient nature of appetite-based interventions and the inflammation-constrained potential of browning agents represents a critical unmet need in the field. Emerging evidence indicates that obese adipose tissue harbors a dysregulated immune landscape dominated by classically activated M1 macrophages, which perpetuate local inflammation and impair metabolic homeostasis [28–30].

Here, we report a previously unrecognized immunomodulatory function of semaglutide (SG): Beyond its established neuroendocrine actions, semaglutide directly engages GLP-1 receptors expressed on adipose tissue macrophages, orchestrating a phenotypic switch toward the alternatively activated M2 anti-inflammatory state. This discovery establishes a mechanistic foundation for rational combination therapy, wherein semaglutide-mediated resolution of adipose inflammation licenses the thermogenic efficacy of browning agents, thereby offering a dual-mechanism approach to achieve durable, non-rebounding weight loss.

Herein, a long-acting composite microneedle patch (LRSG-SG@MN) endowed with adipose-targeting capabilities was meticulously engineered to achieve targeted delivery of rosiglitazone (RSG) and sustained release of semaglutide within adipose tissue (Scheme 1(a)). Specifically, the microneedle patch exhibiting superior mechanical properties and prolonged degradation kinetics was constructed through the precise modulation of hyaluronic acid (HA), gelatin, and gelatinized starch ratios. Semaglutide and rosiglitazone-loaded nano-lipid droplets were subsequently

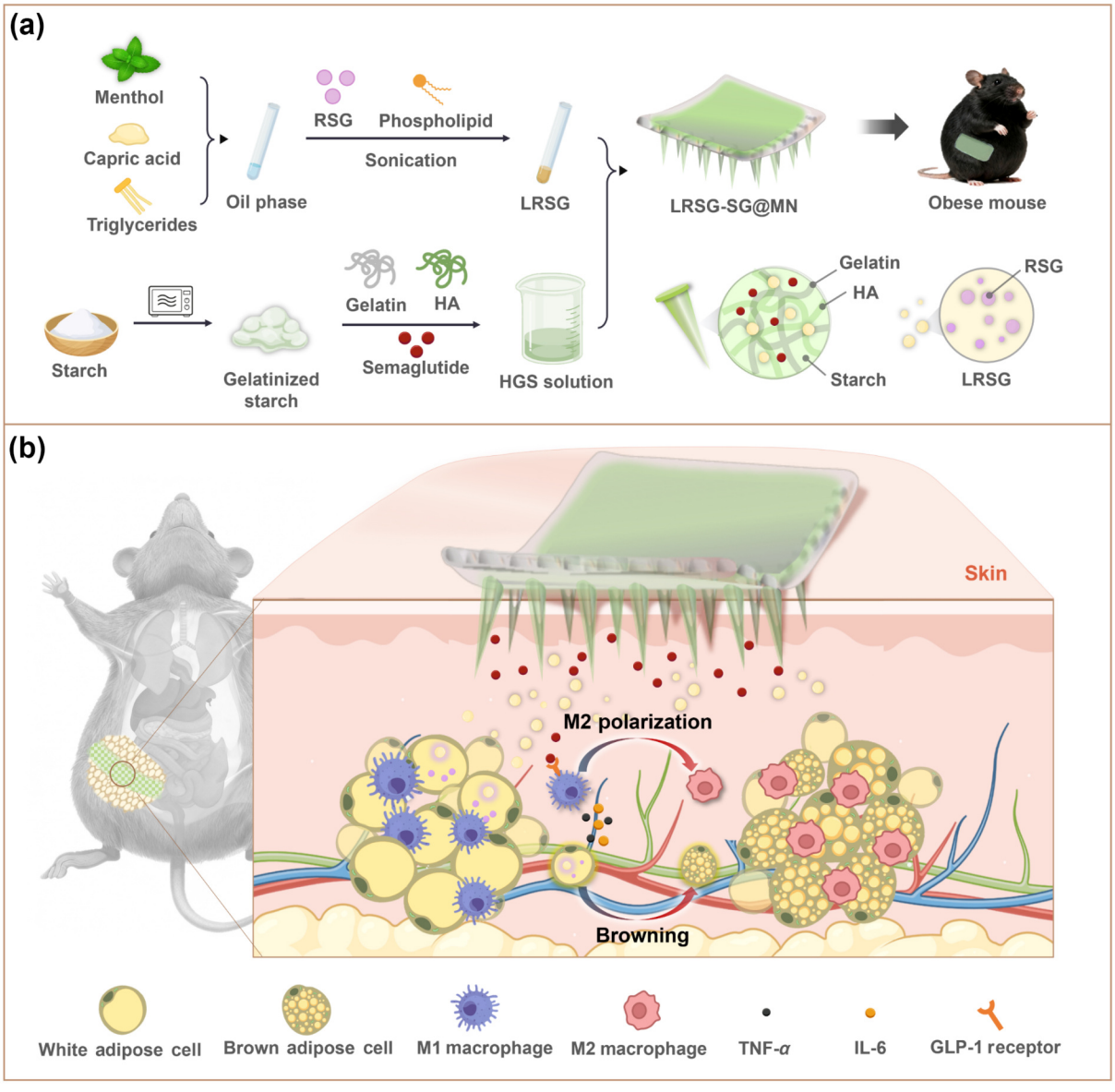

Scheme 1 Design and therapeutic mechanism of the adipose-targeting microneedle patch LRSG-SG@MN for obesity therapy. (a) Scheme illustration of the synthesis process of LRSG-SG@MN. (b) Mechanism of LRSG-SG@MN-mediated browning induction and anti-inflammatory effects in adipose tissue.

incorporated into the microneedles to facilitate sustained drug delivery to subcutaneous adipose tissue. Mechanistically, semaglutide acts upon GLP-1 receptors expressed on macrophages, promoting polarization toward the M2 phenotype, thereby reversing the inflammatory microenvironment of adipose tissue and attenuating intracellular oxidative stress in adipocytes to establish a favorable microenvironment for white adipocyte browning. Concurrently, upon release from the microneedles, rosiglitazone-loaded nano-lipid droplets selectively target adipocytes, markedly enhancing rosiglitazone uptake and accelerating white adipocyte browning (Scheme 1(b)). This cooperative therapeutic strategy demonstrated robust efficacy with excellent safety in a high-fat diet-induced obese mouse model, underscoring its clinical translational potential for obesity management.

2 Results and discussion

2.1 Synthesis and characterization of the microneedle patch LRSG-SG@MN

Rosiglitazone-loaded nano-lipid droplet (LRSG) was synthesized through ultrasonic emulsification [31]. To establish the optimal synthetic parameters, systematic screening of oil phase-to-rosiglitazone feed ratios was conducted. As illustrated in Figs. S1 and S2 in the Electronic Supplementary Material (ESM), a feed ratio of 1 mL:10 mg (oil phase:rosiglitazone), in conjunction with optimized surfactant and oil concentrations, yielded lipid droplets exhibiting superior colloidal stability, enhanced dispersibility, and maximal drug loading capacity. Additionally, a bright optical path was clearly observed for the lipid droplets prepared via the optimal method under laser irradiation, which confirms that the lipid droplets had a uniform particle size distribution centered around 100 nm (Fig. S3 in the ESM). Accordingly, this ratio was selected to prepare LRSG for the subsequent experiments. Transmission electron microscopy (TEM) images depicted the regular spherical morphology of LRSG, and dynamic light scattering (DLS) analysis revealed that LRSG possessed a uniform size of approximately 100 nm and good dispersibility (Figs. 1(a) and 1(b)). Moreover, there was no significant difference in zeta potential between Lipid and LRSG (Fig. S4A in the ESM), and the particle sizes of both Lipid and LRSG remained stable without significant fluctuation during continuous monitoring (Fig. S4(b) in the ESM), which greatly proved the stability of the lipid droplets. Subsequently, the drug-loaded microneedles were prepared through a vacuum defoaming-drying process. To construct the optimal transdermal delivery matrix, various feed ratios of sodium hyaluronate (HA), gelatin (G) and gelatinized starch (S) were tested. As shown in Fig. S5 in the ESM, when the volume ratio of HA:G was 1:2, the composite microneedles exhibited optimal elastic modulus and toughness. Therefore, this ratio was selected to prepare hyaluronic acid-gelatin-gelatinized starch composite microneedles (HGS) and LRSG and semaglutide co-loaded microneedle (LRSG-SG@MN) for subsequent characterization. Scanning electron microscopy (SEM) images depicted the regularly arranged and morphologically intact characteristics of HGS microneedle tips [32, 33]. Meanwhile, the incorporation of LRSG did not alter the microscopic morphology or cause tip fracture, confirming the successful loading of lipid droplets in the microneedle matrix (Fig. 1(c)). As compared to single-component (HA, G) and two-component (HG) microneedles, the three-component HGS microneedles showed superior compression resistance and elastic modulus (Figs. 1(d) and 1(e), and Fig. S6 in the ESM) and rheological properties (highest storage modulus G', Fig. 1(f)), which significantly enhanced the structural stability of the microneedles. Subsequently, to evaluate the practical application potential of the microneedles, skin penetration experiments were performed [34]. As shown in Figs. 1(g) and 1(h), the HGS microneedles could leave clear array marks on porcine skin surface, and the regular needle hole structures observed in tissue sections confirmed their successful penetration of the stratum corneum barrier. Furthermore, the *in vitro* release kinetics studies demonstrated that the HGS microneedles achieved a cumulative drug release of 45.8% over a 24 h period (Fig. S7 in the ESM). In comparison with the control group, the HGS microneedles exhibited a more stable degradation profile and sustained-release characteristics (Fig. 1(i)), which could be attributed to the dense network architecture formed by the ternary components that effectively retarded matrix degradation.

2.2 Evaluation of LRSG-mediated adipocyte browning

Subsequently, functional validation of the adipose-targeted delivery system (LRSG) was conducted at the cellular level. Initially, an experimental concentration of 25 μg/mL for rosiglitazone was determined via cytotoxicity assays, as this concentration demonstrated no significant cytotoxicity toward adipocytes (Fig. S8 in the ESM). To evaluate the cellular affinity differences of lipid droplet carriers, confocal microscopy was used to detect the endocytosis efficiency of 1,1'-dioctadecyl-3,3,3',3'-tetramethylindodicarbocyanine (DID)-labeled lipid droplets in human umbilical vein endothelial cells (HUVECs), pre-adipocytes (3T3-L1), and mature adipocytes. As illustrated in Fig. 2(a), compared with HUVECs, the endocytosis ability of 3T3-L1 cells and mature adipocytes to lipid droplets was significantly enhanced, and the intracellular DID fluorescence signal intensity of mature adipocytes was the highest at the same time point, which indicated that mature adipocytes can internalize lipid droplets more rapidly and abundantly and exhibit a stronger preference for lipid. This phenomenon was attributed to the matching between the lipid components of the carriers and the membrane structure and intracellular lipid metabolism characteristics of adipocytes, giving them natural adipocyte-selective affinity, which could be efficiently taken up by adipocytes via passive targeting.

Subsequently, Oil Red O staining was used to detect intracellular lipid droplet morphological changes. As shown in Figs. 2(b) and 2(c), compared with the phosphate-buffered saline (PBS) group and Lipid group, the lipid droplet size in adipocytes of the LRSG treatment group was significantly reduced, and the lipid droplet number was obviously increased, which exhibited the typical phenotypic characteristics of brown adipocytes. Moreover, intracellular mitochondrial content was assessed by Mito-Tracker Red, a mitochondrion-selective fluorescent probe, following different treatments. As shown in Figs. 2(d) and 2(e), the red fluorescence intensity of the LRSG group was significantly higher than that of the PBS group and the Lipid group, indicating that LRSG could markedly upregulate the intracellular mitochondrial content in adipocytes, thus accelerating the progression of adipocyte browning. To further verify this conclusion, transmission electron microscopy was used to observe the specific ultrastructure within adipocytes. As shown in Fig. 2(f), a remarkable increase in mitochondrial content accompanied by lipid droplet

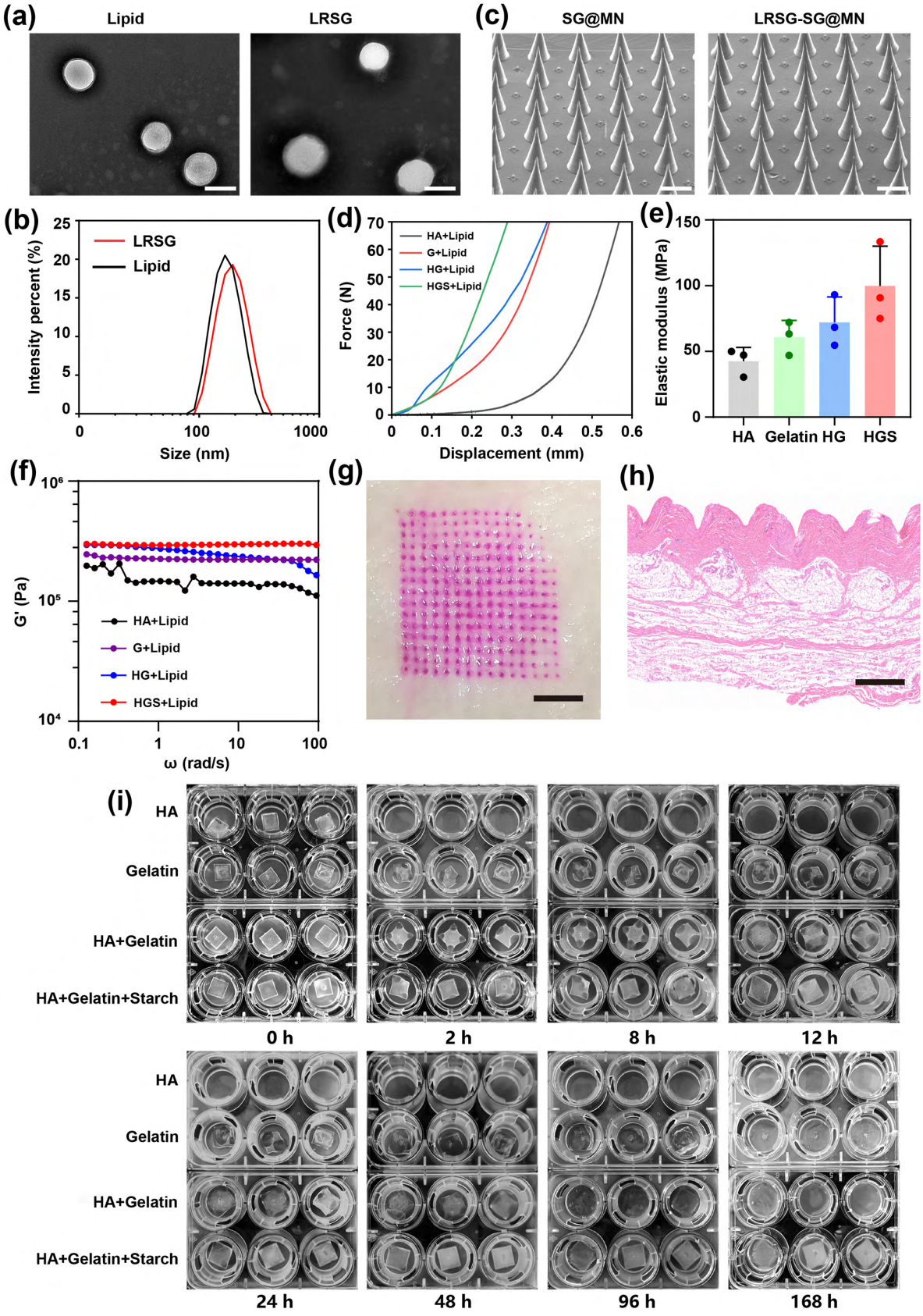

Figure 1 Characterization of the patch LRSG-SG@MN. (a) Representative TEM images of Lipid and LRSG. Scale bars: 100 nm. (b) Hydrated size of Lipid and LRSG. (c) Representative SEM images of SG@MN and LRSG-SG@MN. Scale bars: 500 μm. (d) Force-displacement profiles, (e) elastic modulus (n = 3 independent experiments per group), and (f) storage modulus (G') of the microneedles with distinct formulations. (g) Representative images of punctured porcine skin. Scale bar: 4 mm. (h) H&E staining of punctured porcine skin. Scale bar: 500 μm. (i) Time-lapse images showing degradation of microneedles.

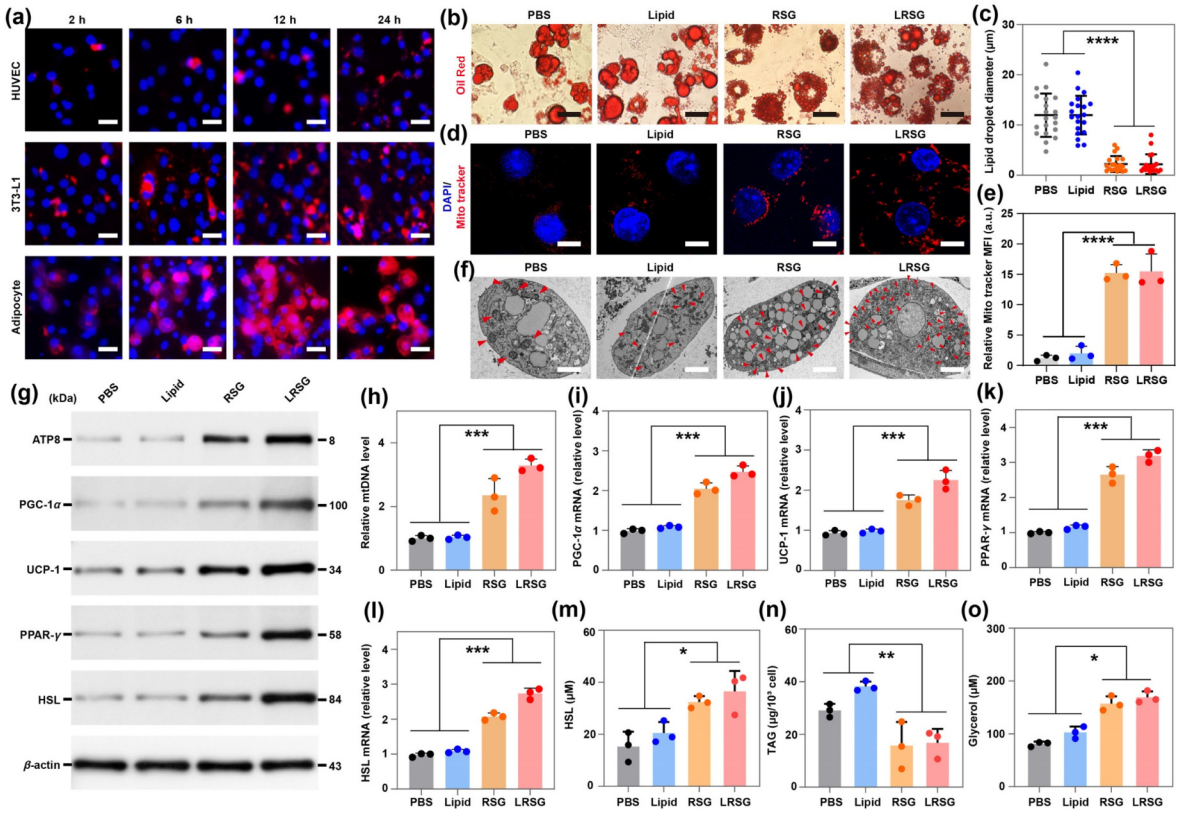

Figure 2 LRSG-mediated adipocyte browning. (a) Endocytosis analysis of HUVEC, 3T3-L1 and Adipocyte. Scale bars: 50 μm. (b) Oil Red O staining of Adipocyte after different treatments. Scale bars: 100 μm. (c) The corresponding quantitative of lipid droplet diameter in panel (b) (n = 20 examined over 3 independent experiments). (d) Representative images of mitochondrial staining in adipocytes after different treatments. Scale bars: 10 μm. (e) The corresponding quantitative mean fluorescence intensity in panel (d) (n = 3 independent experiments per group). (f) Representative TEM images of adipocytes after different treatments. Scale bars: 10 μm. (g) Western blot analysis of ATP8, PGC-1α, UCP-1, PPAR-γ and HSL expression in adipocyte after different treatments. Expressions of (h) mtDNA, (i) PGC-1α, (j) UCP-1, (k) PPAR-γ, and (l) HSL in adipocyte after different treatments. (m) HSL, (n) TAG, and (o) glycerol level in adipocyte after different treatments. Statistical significance was calculated using the one-way ANOVA with Tukey post-hoc analysis. *P < 0.05, **P < 0.01, ***P < 0.001, ****P < 0.0001. The values are presented as mean ± standard error of the mean (s.e.m.).

miniaturization was distinctly observed in adipocytes following LRSG treatment, providing intuitive evidence for the enhanced effect of LRSG on adipocyte browning.

Thereafter, to elucidate the molecular mechanism of LRSG-induced adipocyte browning, quantitative polymerase chain reaction (qPCR) and Western blot techniques were used to detect the expression levels of browning-related genes and proteins in adipocytes. As shown in Figs. 2(g)–2(k), the mRNA and protein expression levels of the browning core regulatory factor PPAR-γ and the thermogenic key protein uncoupling protein 1 (UCP-1) in the LRSG group were significantly higher than those in the PBS and Lipid groups, while the expression of mitochondrial biogenesis-related gene ATP8 and mitochondrial function-related gene peroxisome proliferator-activated receptor gamma coactivator 1-alpha (PGC-1α) showed a significant upregulation trend. This experimental observation further corroborated the potentiating effect of LRSG on adipocyte browning. In addition, significantly upregulated expression of the lipid metabolism-related gene hormone-sensitive lipase (HSL) was detected after LRSG treatment (Figs. 2(g) and 2(l)), and the concentrations of triacylglycerol (TAG) (lipid metabolism substrates) and glycerol (lipid metabolism products) changed significantly (Figs. 2(m)–2(o)). This result was consistent with the high metabolic activity characteristics of browning cells, further confirming the advantage of lipid droplet carrier-mediated RSG delivery in enhancing adipocyte browning.

2.3 Assessment of SG-mediated anti-inflammatory effects

The efficient induction of adipocyte browning not only depends on the activation of browning pathways but also requires the relief of inflammatory microenvironment inhibition. M2-type polarization of macrophages is a key link in alleviating adipose tissue inflammation, and SG can regulate this process by acting on GLP-1 receptors on the macrophage surface. We first evaluated the regulatory effect of serial concentrations of SG on macrophage polarization by flow cytometry. As illustrated in Fig. S9 in the ESM, no significant cytotoxicity was detected in macrophages treated with SG across the concentration range of 0 to 50 μg/mL. Subsequently, we evaluated the regulatory effect of serial concentrations of SG within this range on macrophage polarization by flow cytometry (Fig. S10 in the ESM). 20 μg/mL SG achieved the most potent efficacy in facilitating M2 macrophage polarization, and was therefore selected for all subsequent experiments.

To investigate the effect of GLP-1 receptor activation on M2 macrophage polarization, macrophages were analyzed by flow cytometry. Flow cytometric results showed that the proportion of M2 macrophages was significantly increased while the proportion of M1 macrophages was significantly decreased in the SG group. In contrast, the proportion of M2 macrophages in the SG+exendin(9-39) (GLP-1R antagonist) group was significantly lower than that in the SG group, demonstrating that SG-induced M2 macrophage

polarization was associated with GLP-1R on macrophages (Fig. S11 in the ESM). As shown in Figs. 3(a)–3(d), compared with the PBS group and MN group, macrophages in the semaglutide-loaded microneedle (SG@MN) group showed obvious M2-type polarization characteristics, with M1-type macrophages decreasing from 40.9% to 27.8% and M2-type macrophages increasing from 18.8% to 52.4%, indicating that SG@MN had significant macrophage polarization regulation ability.

Further detection of cytokines secreted by macrophages showed that the concentrations of pro-inflammatory factors interleukin-6 (IL-6) and tumor necrosis factor-α (TNF-α) in the SG@MN group were significantly lower than those in the PBS group and MN group (Figs. 3(e) and 3(f)), and its anti-inflammatory effect was comparable to that of the free SG group, confirming that SG@MN could effectively exert anti-inflammatory effects.

Subsequently, we co-cultured adipocytes with the supernatant of macrophages treated with PBS, MN, SG and SG@MN, and detected the changes in intracellular ROS levels in adipocytes via confocal microscopy imaging. As shown in Fig. 3(g) and Fig. S12 in the ESM, the fluorescence intensity of ROS in adipocytes from the SG and SG@MN groups was significantly lower than that in the PBS and MN groups, which indicated that the secretions from macrophages treated with SG and SG@MN could suppress the inflammatory response in adipocytes. Furthermore, the intracellular C-reactive protein (CRP) protein levels in adipocytes were quantified by Western blot analysis, while the secreted levels of ADIPOQ and monocyte chemoattractant protein-1 (MCP-1) were determined by enzyme-linked immunosorbent assay (ELISA). The experimental results demonstrated that compared with the PBS group and MN group, the CRP expression in adipocytes after SG@MN treatment was significantly reduced (Fig. 3(h)), ADIPOQ expression showed a significant upward trend (Fig. S13 in the

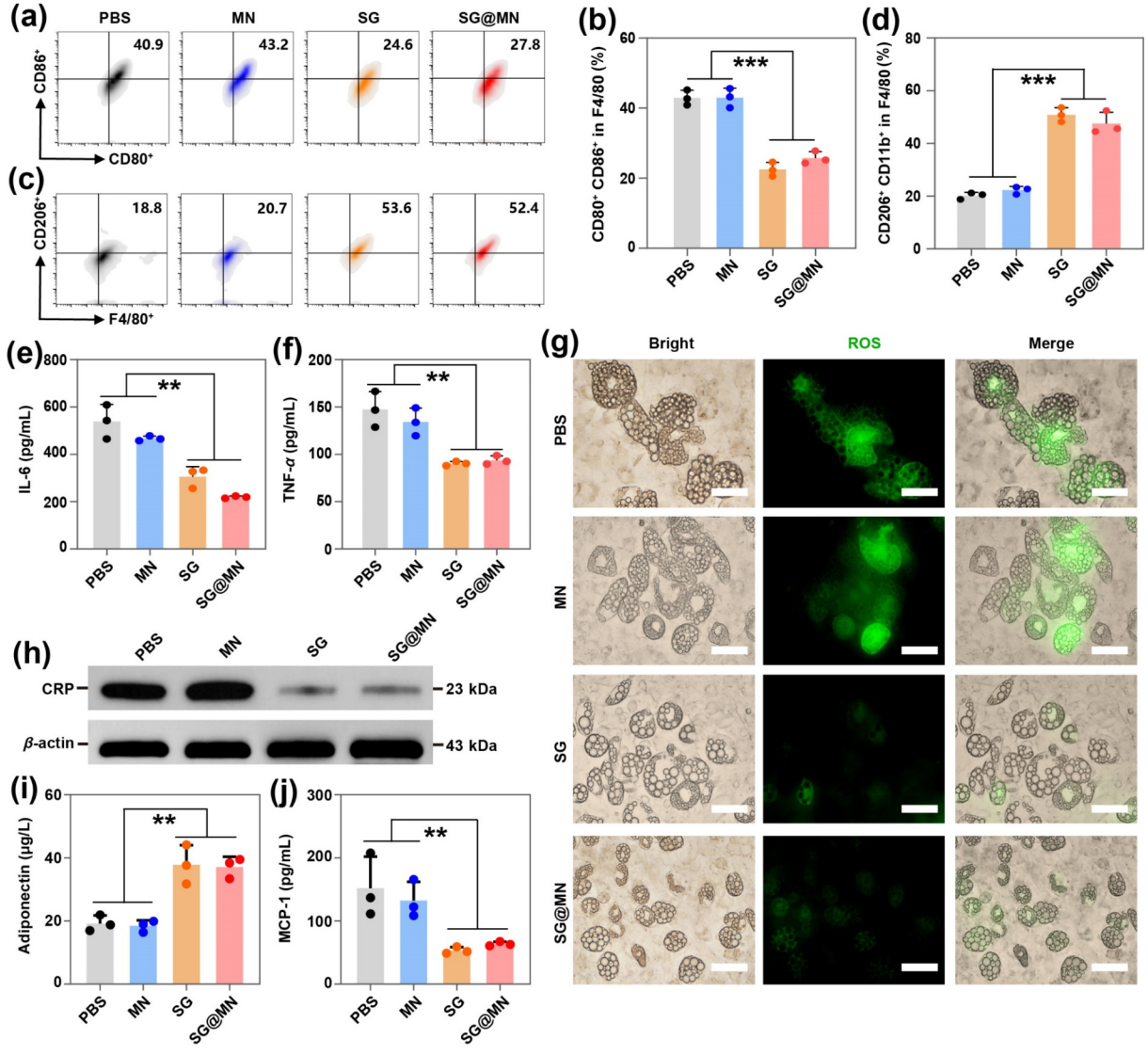

Figure 3 SG-mediated anti-inflammatory effects. (a) M1 phenotypes analysis of macrophage after different treatments by flow cytometry and (b) the corresponding quantitative results (n = 3 independent experiments per group). (c) M2 phenotypes analysis of macrophage after different treatments by flow cytometry and (d) the corresponding quantitative results (n = 3 independent experiments per group). (e) IL-6 and (f) TNF-α levels in the macrophage supernatants (n = 3 independent experiments per group). (g) ROS fluorescence images of adipocytes co-incubated with supernatant from differentially treated macrophages. Scale bar: 200 μm. (h) Western blot analysis of CRP expression in adipocyte after different treatments. (i) Adiponectin and (j) MCP-1 levels in adipocyte supernatants (n = 3 independent experiments per group). Statistical significance was calculated using the one-way ANOVA with Tukey post-hoc analysis. $^{**}P < 0.01$, $^{***}P < 0.001$. The values are presented as mean ± s.e.m.

ESM), and pro-inflammatory cytokine MCP-1 secretion was reduced while anti-inflammatory cytokine ADIPOQ secretion was significantly increased (Figs. 3(i) and 3(j)). Collectively, these findings demonstrate that SG@MN effectively attenuated adipocyte inflammation by modulating macrophage polarization.

2.4 Detection of the targeting and retention capabilities of LRSG-SG@MN *in vivo*

To determine the adipose tissue penetration capacity of LRSG-SG@MN, microneedles loaded with fluorescently labeled materials were used to puncture *ex vivo* porcine skin, as shown in Fig. 4(a). Nile Red-labeled lipid droplets infiltrated into the adipose layer, while sodium fluorescein was retained within the cutaneous layer, which demonstrated that the lipid droplet-based material exhibited a prominent penetration capability toward adipose tissue. Subsequently, after confirming the successful establishment of high-fat diet (HFD)-induced obese mouse model, the obese mice were randomly divided into 4 groups and received treatment of Cy5.5, Cy5.5-Lipid, Cy5.5@MN and Cy5.5-Lipid@MN, respectively. As shown in Figs. 4(b) and 4(c), the fluorescence signal of adipose tissues treated with Cy5.5 solution and Cy5.5-Lipid faded away within 2 days, displaying the short stay of Cy5.5 and Cy5.5-Lipid in adipose tissue. By contrast, the fluorescence signals were evidently detected in the adipose tissues treated with Cy5.5@MN and Cy5.5-Lipid@MN for up to 6 days, indicating that the designed microneedle patch demonstrated an outstanding capacity for long-term sustained retention. Moreover, to further elucidate the intra-adipose distribution of Lipid@MN, adipose tissues were harvested from each group on day 2 post-administration for fluorescence detection. As shown in Figs. 4(d) and 4(e), the intensity of retained fluorescence in the epididymal white adipose tissue of mice administered with Cy5.5-Lipid@MN was significantly higher than that in the Cy5.5@MN group. This was attributed to the intrinsic adipose-targeting ability of lipid droplets, which improved the cellular internalization of Cy5.5 encapsulated in the droplets.

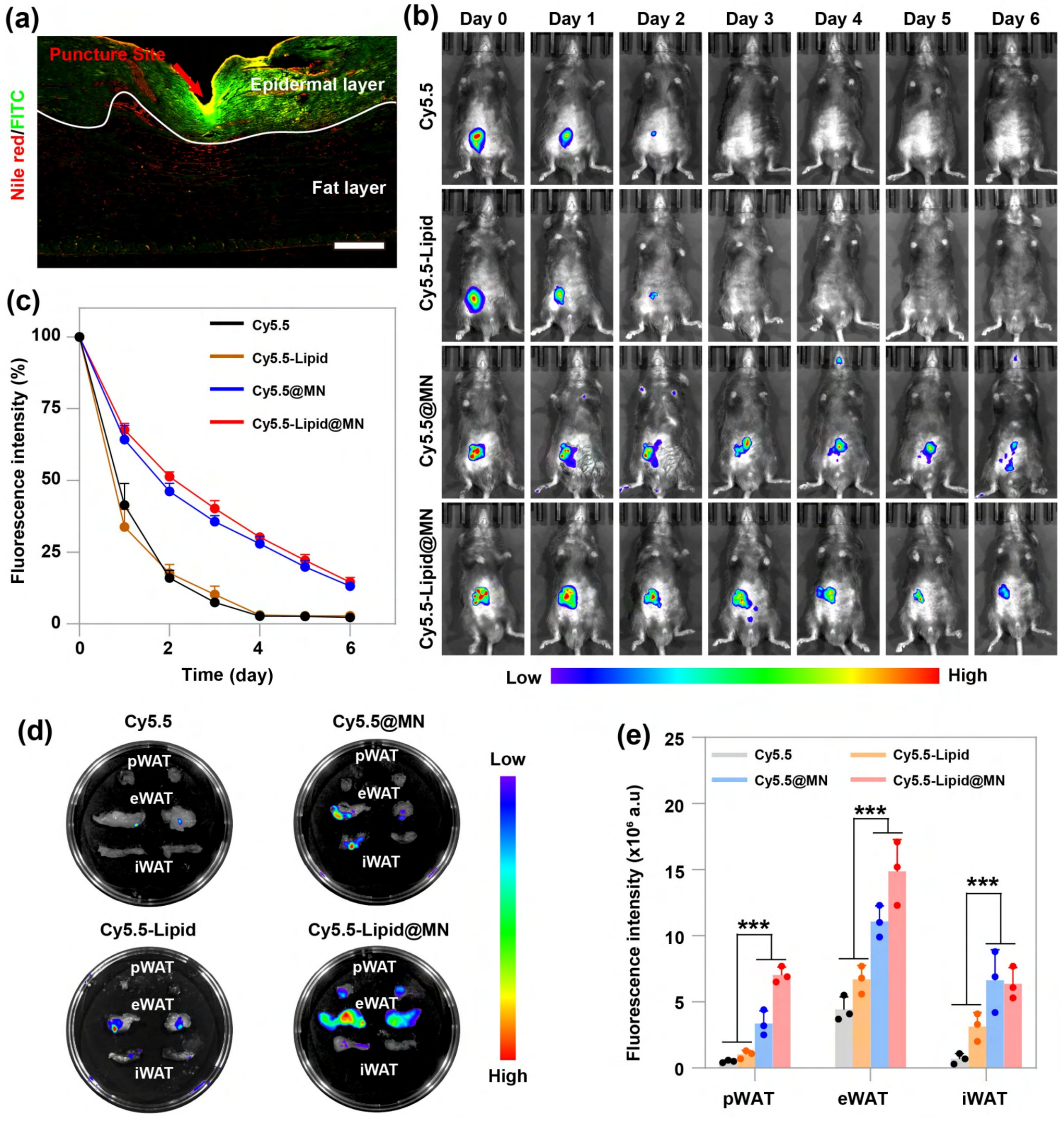

Figure 4 Adipose-targeting and skin penetrability of LRSG-SG@MN. (a) *In vitro* porcine skin penetration capability of different materials delivered via microneedles. Scale bar: 100 μm. (b) *In vivo* fluorescence distribution of Cy5.5, Cy5.5-Lipid, Cy5.5@MN, and Cy5.5-Lipid@MN at different time points and (c) the corresponding quantification of mean fluorescence intensity (n = 3 biologically independent mice per group). (d) *Ex vivo* Cy5.5 fluorescence imaging of the fat tissue collected from the mice with different treatments at day 2 and (e) the corresponding quantitative results (n = 3 biologically independent mice per group). Statistical significance was calculated using the one-way ANOVA with Tukey post-hoc analysis. ***P < 0.001. The values are presented as mean ± s.e.m.

2.5 Assessment of LRSG-SG@MN-mediated anti-obesity effects

Furthermore, the therapeutic efficacy of LRSG-SG@MN was evaluated on the established HFD-induced obese mouse model (Fig. 5(a)). The obese mice were treated with different formulations (PBS, LRSG@MN, SG@MN, and LRSG-SG@MN), and the body weight was applied to monitor the progression of obesity after different treatments. Noteworthily, similar to the control group, LRSG@MN treatment failed to effectively suppress HFD-induced weight gain, suggesting that the browning potential of RSG might be impaired under the chronic inflammatory environment of obesity (Fig. 5(b) and Fig. S14 in the ESM). Meanwhile, the photograph of treated mice and *ex vivo* adipose tissue images further confirmed that LRSG-SG@MN treatment significantly lowered whole-body fat accumulation in mice (Fig. 5(c)). Moreover, magnetic resonance imaging (MRI) imaging and the weights of excised inguinal white adipose tissue (iWAT), epididymal white adipose tissue (eWAT), and perirenal adipose tissue (pWAT) further showed intuitive evidence of fat mass reduction with the treatment of LRSG-SG@MN (Figs. 5(d) and 5(e)).

To further elucidate the anti-obesity mechanism, we characterized the energy expenditure and metabolic status to monitor the changes in metabolic capacity of mice following different treatments. As shown in Figs. 5(f)–5(h), as compared to the control group, significantly elevated oxygen consumption (VO_2), carbon dioxide production (VCO_2), and increased respiratory exchange rate (RER) were simultaneously detected in the mice treated with LRSG-SG@MN, demonstrating that LRSG-SG@MN could activate systemic metabolism and induce thermogenesis for potentiating the energy expenditure. Subsequently, to investigate the glucose tolerance status of mice, an intraperitoneal glucose tolerance test (GTT) was performed. As displayed in Fig. 5(i), mice treated with LRSG@MN, SG@MN and LRSG-SG@MN all exhibited a certain degree of attenuation in blood glucose fluctuations after intraperitoneal glucose injection. The LRSG-SG@MN intervention conferred the most pronounced metabolic benefits, manifesting as decelerated postprandial glucose accretion, attenuated glycemic fluctuation in response to intraperitoneal glucose administration, and lowered baseline glycemic levels. These observations substantiated that LRSG-SG@MN administration markedly augments glucose homeostatic capacity and exerts a robust protective effect against the onset and progression of high-fat diet-induced diabetic pathology. Then, the Oil Red O and hematoxylin and eosin (H&E) staining of liver and adipose tissues were applied to evaluate the pathological changes of metabolic organs. As shown in Figs. 5(j)–5(l), the most severe reduction of lipid accumulation and amelioration of hepatic steatosis were found in the mice with the treatment of LRSG-SG@MN, which was observably better than other treatment groups. Furthermore, it has been well documented that SG possesses central anorexigenic effects. Consistent with this, the monitoring of daily food intake showed that the intake was significantly reduced in the SG@MN and LRSG-SG@MN groups (Fig. S15 in the ESM). This appetite suppression partially explained why the SG@MN group could exhibit weight control even without direct browning induction. More importantly, there was no statistically significant difference in daily food intake between mice treated with SG@MN and LRSG-SG@MN, whereas the adipocyte size in the LRSG-SG@MN treatment group was significantly smaller than that in the SG@MN treatment group (Fig. 5(m)). These results comprehensively elaborated that LRSG-SG@MN could regulate the adipocyte metabolism to a thermogenic phenotype and efficiently reinforce the improvement of liver function for activating the systemic metabolic reprogramming and inhibiting the progression of obesity. In addition, no significant changes in the blood biochemical and blood routine indexes (Fig. S16 in the ESM) of obese mice with different treatments were detected, revealing that LRSG-SG@MN had favorable biological safety and would not cause systemic toxicity to mice. Besides, the H&E staining of major organs, such as heart, spleen, lung, and kidney, of mice with different treatments (PBS, LRSG@MN, SG@MN, and LRSG-SG@MN) showed negligible difference (Fig. S17 in the ESM), demonstrating the satisfactory biocompatibility of LRSG-SG@MN.

2.6 Evaluation of the inflammation and browning mechanism in adipose tissue by transcriptome analysis

To elucidate the mechanism underlying the therapeutic effect of LRSG-SG@MN against obesity, we performed transcriptomic profiling of adipose tissue treated with LRSG-SG@MN versus PBS control, which revealed that inflammation-related signaling pathways were significantly inhibited, while browning-related signaling pathways were markedly upregulated. Principal component analysis (PCA) revealed a clear separation in global gene expression patterns between the two groups (Fig. 6(a)), confirming a profound transcriptional reprogramming induced by LRSG-SG@MN treatment. The LRSG-SG@MN-mediated therapy resulted in 499 differentially expressed genes (DEGs), comprising 100 up-regulated and 399 downregulated transcripts (Fig. 6(b)). Particularly, the upregulated genes included *Serpina6* and *Coa7*, encoding anti-inflammatory and mitochondrial function, while the downregulated genes, such as *Sesn2*, *Soat2*, *Dusp5*, *Atf3* and *Zfp36* were related to pro-inflammatory signal pathway (Fig. 6(c)). Gene Ontology (GO) and Kyoto Encyclopedia of Genes and Genomes (KEGG) enrichment analysis revealed that pathway alterations in LRSG-SG@MN-treated adipose tissue were significantly involved in regulation of inflammatory pathway, brown fat cell differentiation and fatty acid metabolic process (Figs. 6(d) and 6(e)). Complementary GO and Gene Set Enrichment Analysis (GSEA) further demonstrated that LRSG-SG@MN intervention significantly modulated core biological pathways in adipose tissue (Figs. 6(f) and 6(g)), particularly for those related to inflammatory response and mitochondrial function (e.g., mitochondrial respiratory chain complex I assembly). Furthermore, KEGG-GSEA found that the pathways related to immunosuppression (e.g., JAK-STAT signaling pathway, MAPK signaling pathway, and NF-kappa B signaling pathway) and adipocyte browning (e.g., PPAR signaling pathway) were significantly changed (Figs. 6(h)–6(k)), confirming that LRSG-SG@MN treatment could concomitantly attenuate tissue inflammation and potentiate adipocyte browning.

2.7 Assessment of LRSG-SG@MN-mediated cooperative browning and anti-inflammatory effects *in vivo*

Guided by the results of the aforementioned transcriptomic analysis, we further performed validation experiments to confirm that LRSG-SG@MN effectively induces adipose tissue browning and ameliorates the inflammatory microenvironment in the adipose tissue of obese mice. As shown in Figs. 7(a)–7(d), the level of adiponectin (ADIPOQ, anti-inflammatory factor) remarkably

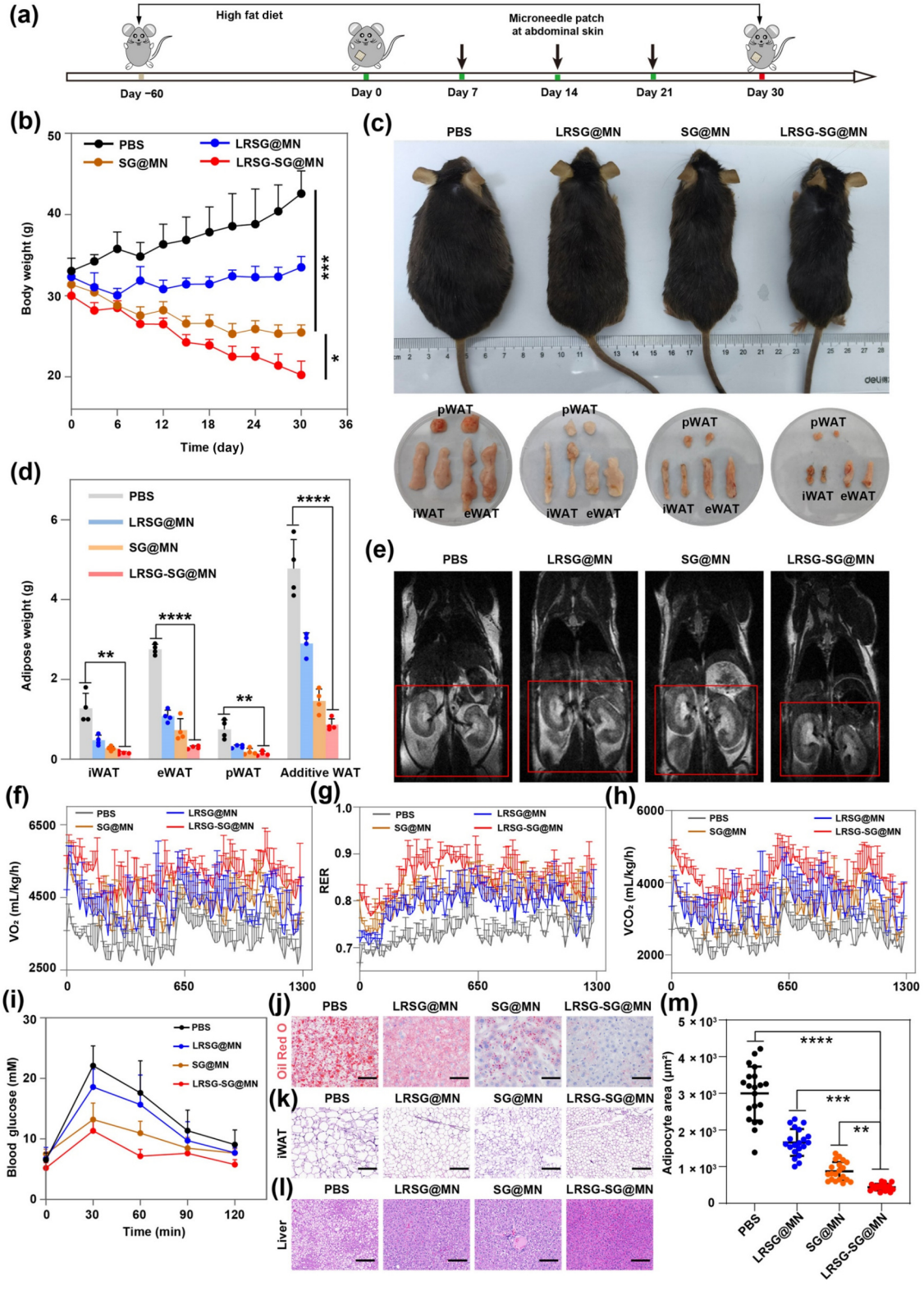

Figure 5 Evaluation of the therapeutic effects of LRSG-SG@MN on the high-fat diet-induced obesity model. (a) Schematic illustration of the therapeutic profile of obese mice. (b) Body weight of obese mice during the treatment (n = 4 biologically independent mice per group). (c) Photograph of HFD-induced obese mice and adipose tissue after different treatments. (d) Adipose tissue weight of obese mice after different treatments (n = 4 biologically independent mice per group). (e) Representative MRI images of obese mice after different treatments. (f) VO_2, (g) RER, and (h) VCO_2 of obese mice after different treatments (n = 3 biologically independent mice per group). (i) GTT of obese mice (n = 3 biologically independent mice per group). (j) Oil Red O staining of liver after different treatments. Scale bars: 200 μm. (k) H&E staining of adipose tissue after different treatments. Scale bars: 100 μm. (l) H&E staining of liver after different treatments. Scale bars: 500 μm. (m) The corresponding quantitative results of adipocyte area in adipose tissue after different treatments (n = 20 examined over 3 independent mice). Statistical significance was calculated using the one-way ANOVA with Tukey post-hoc analysis. $^*P < 0.05$, $^{**}P < 0.01$, $^{***}P < 0.001$, $^{****}P < 0.0001$. The values are presented as mean ± s.e.m.

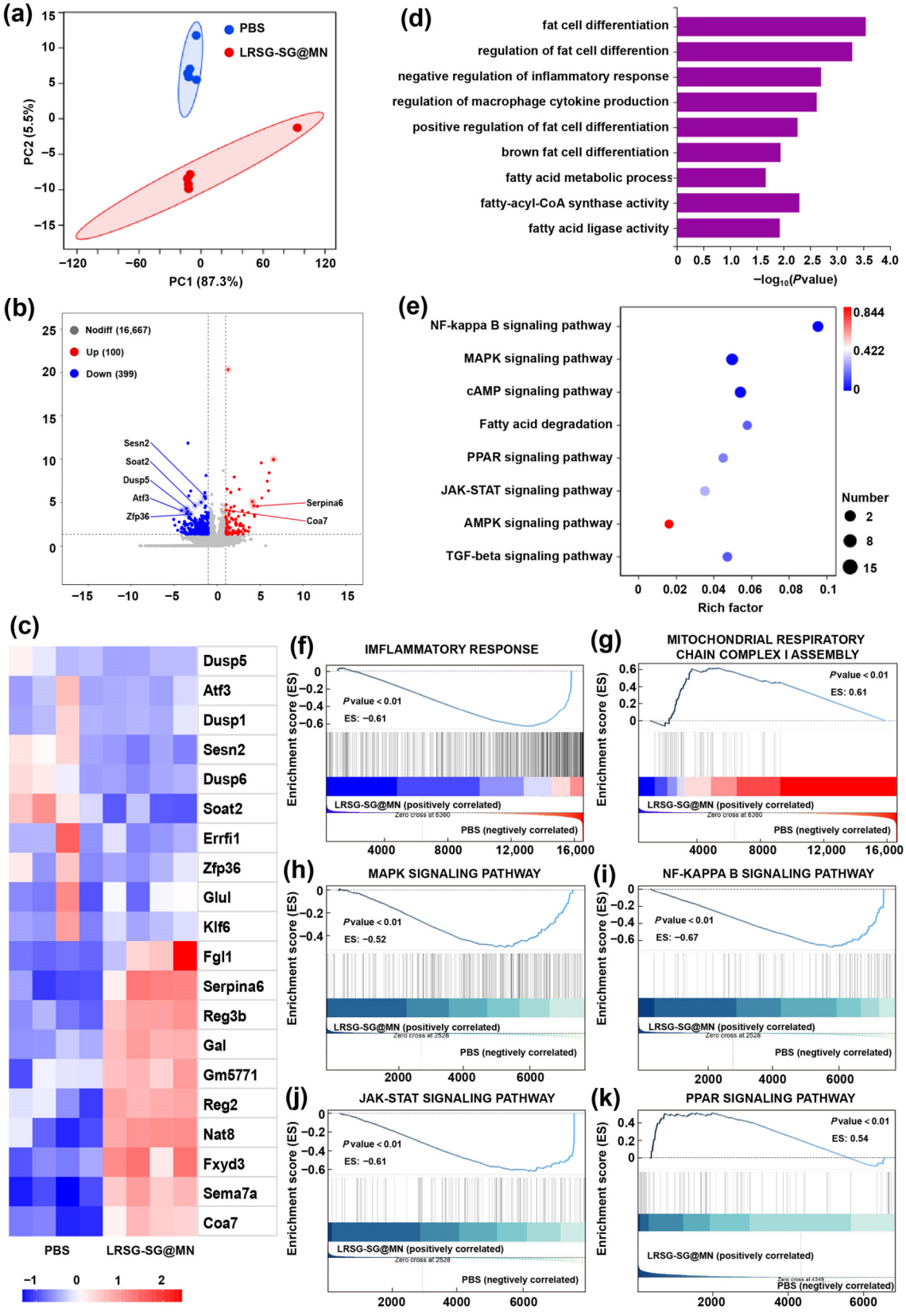

Figure 6 Evaluation of the inflammation and browning mechanism in adipose tissue by transcriptome analysis. (a) Principal component analysis plotting of two groups of transcripts (n = 5 biologically independent mice per group). (b) Volcano plot of genomics data for adipose tissue treated with PBS or LRSG-SG@MN. (c) Heat map visualizing hierarchical clustering of the downregulated and upregulated genes in adipose tissue treated with PBS or LRSG-SG@MN (n = 5 biologically independent mice per group). (d) The GO enrichment analysis and (e) KEGG enrichment analysis of adipose tissue with the treatment of LRSG-SG@MN. (f) GSEA and (g) GO enrichment, and (h)–(k) KEGG enrichment in adipose tissue treated with PBS or LRSG-SG@MN.

increased in the LRSG-SG@MN group of mice compared with the PBS and LRSG@MN groups, while MCP-1 and CRP (inflammatory factors) were significantly reduced. Moreover, flow cytometric profiling of adipose tissue revealed that LRSG-SG@MN treatment induced a profound shift in macrophage polarization with the suppression of M1 macrophages ($F4/80^+CD80^+CD86^+$), decreasing from 42.2% (PBS group) to 17.2% (Figs. 7(e) and 7(f)). Conversely, LRSG-SG@MN treatment significantly increased the proportion of M2 macrophages ($CD11b^+F4/80^+CD206^+$) to 21.9% (Figs. 7(e) and 7(g)), which was significantly higher than other groups (PBS: 11.2%; LRSG@MN: 14.2%; SG@MN: 18.8%). Simultaneously, ELISA detection showed that the secretion of pro-inflammatory cytokines (TNF-α, IL-6) in the LRSG-SG@MN group was much lower than that in other groups (Figs. 7(h) and 7(i)).

Furthermore, the browning effect of LRSG-SG@MN *in vivo* was evaluated, and the expression of browning markers was detected by immunofluorescence staining. As shown in Figs. 7(j)–7(m), compared with the PBS and SG@MN groups, LRSG@MN treatment could significantly increase the expression of PPAR-γ and UCP-1. More importantly, higher expression levels of PPAR-γ and UCP-1 were detected in adipose tissue of mice treated with LRSG-SG@MN compared with the LRSG@MN treatment group, which demonstrated that amelioration of the inflammatory microenvironment by SG contributes to the enhanced adipocyte browning effect mediated by RSG.

Since mitochondrial biogenesis is closely associated with adipose browning, the relative mitochondrial DNA (mtDNA) content and PGC-1α expression were first evaluated. Subsequently, the relative mtDNA content and the expression levels of PGC-1α in adipose tissue of mice following different treatments were assessed, to further characterize the extent of adipocyte browning. Compared with the PBS group, both the LRSG@MN and LRSG-SG@MN groups showed a certain degree of upregulation in these indicators, while the extent of upregulation in the LRSG@MN group was significantly lower than that in the LRSG-SG@MN group (Figs. 7(n) and 7(o)). These results consistently demonstrated that LRSG-SG@MN-elicited alleviation of the inflammatory microenvironment in adipose tissue markedly potentiates the efficiency of adipocyte browning.

Subsequently, the lipolytic metabolism was studied in detail. As expected, the LRSG-SG@MN group observably improved the HSL expression and reduced the adipose TAG content with elevated glycerol levels (Figs. 7(p)–7(r)), which was significantly better, demonstrating that LRSG-SG@MN can accelerate adipocyte browning by alleviating adipose tissue inflammation, thereby effectively promoting lipid metabolism and suppressing excessive lipid accumulation in adipocytes. Taken together, LRSG-SG@MN showed the favorable ability to eliminate the inflammatory barrier and activate adipose browning, which were in favor of eliciting powerful metabolic reprogramming and anti-obesity efficacy.

3 Conclusions

In conclusion, this study establishes a cooperative therapeutic paradigm for durable obesity management through the development of an adipose-targeted, long-acting nanocomposite microneedle patch (LRSG-SG@MN). By integrating sustained-released semaglutide with adipose-targeted nano-lipid droplet delivery of rosiglitazone, this platform achieves precise immuno-metabolic modulation. Our findings unveil the non-central immunomodulatory function of semaglutide, as direct activation of GLP-1 receptors on adipose tissue macrophages drives M2 polarization, resolving chronic inflammation and relieving its suppressive effects on thermogenesis. Concurrently, rosiglitazone-loaded nano-lipid droplets are selectively internalized by adipocytes, with browning efficiency markedly potentiated following inflammatory amelioration. This dual-drug co-delivery system overcomes the fundamental limitations of conventional monotherapies, specifically weight rebound associated with central appetite suppression and inflammation-constrained browning efficacy. In high-fat diet-induced obese mice, the LRSG-SG@MN platform demonstrated robust combinatorial outcomes, significantly activating thermogenic metabolic pathways, markedly reducing adiposity, and effectively ameliorating glucolipid metabolic disorders. Notably, the system exhibited superior weight maintenance capacity following treatment cessation without significant rebound, achieving durable anti-obesity outcomes. These results substantiate that adipose tissue inflammatory reprogramming coupled with browning induction via nanocomposite microneedle-mediated delivery represents a transformative strategy for sustainable obesity management, with broad implications for the design of next-generation nanomedicine platforms targeting metabolic diseases.

4 Experimental

4.1 Materials

Starch was purchased from the local market. Ethanol was purchased from Sinopharm Group. Gelatin, soybean phospholipids, insulin, 3-isobutyl-1-methylxanthine (IBMX), dexamethasone (DXM), RSG, and capric acid were purchased from Aladdin. SG and sodium HA (M_w 8k–15k) were purchased from Bide Pharmatech Ltd. Menthol was purchased from Tokyo Chemical Industry. Cyanine 5.5 (Cy5.5), Nile Red, mouse HSL kit were purchased from Shanghai Macklin Biochemical Co., Ltd. Oil Red O, TAG content assay kit, 2',7'-dichlorodihydrofluorescein diacetate (DCFH-DA), and DID were purchased from Beijing Solarbio Science & Technology Co., Ltd. Amplex Red glycerol assay kit was purchased from Beyotime Biotechnology. Puromycin and Dulbecco's modified Eagle medium (DMEM) were purchased from Sperikon Life Science and Biotechnology Co., Ltd. Fetal calf serum and trypsin were purchased from GIBCO Invitrogen Corp. APC-anti-F4/80, PE-anti-CD11b, APC-anti-CD86, FITC-anti-F4/80, PE-anti-CD80, FITC-anti-CD206 were all purchased from ThermoFisher Scientific (USA). Transwell chamber was purchased from SAINING Biotechnology. ELISA kits of IL-6 and TNF-α were all purchased from Beijing Solarbio Science and Technology Co., Ltd.

4.2 Construction and characterization of LRSG

Lipid droplets loaded with RSG were prepared via the ultrasonic emulsification method. First, soybean phospholipids were mixed with ethanol at a mass ratio of 5:1, and the mixture was dissolved in ultrapure water to obtain a surfactant. Prior to lipid droplet preparation, menthol and capric acid were mixed at a molar ratio of 2:1 and heated in a 40 °C oil bath to obtain a hydrophobic deep eutectic solvent (DES). The DES was mixed with medium-chain triglycerides at a volume ratio of 1:100, and RSG was incorporated into the mixture. The resulting mixture was heated and stirred in a

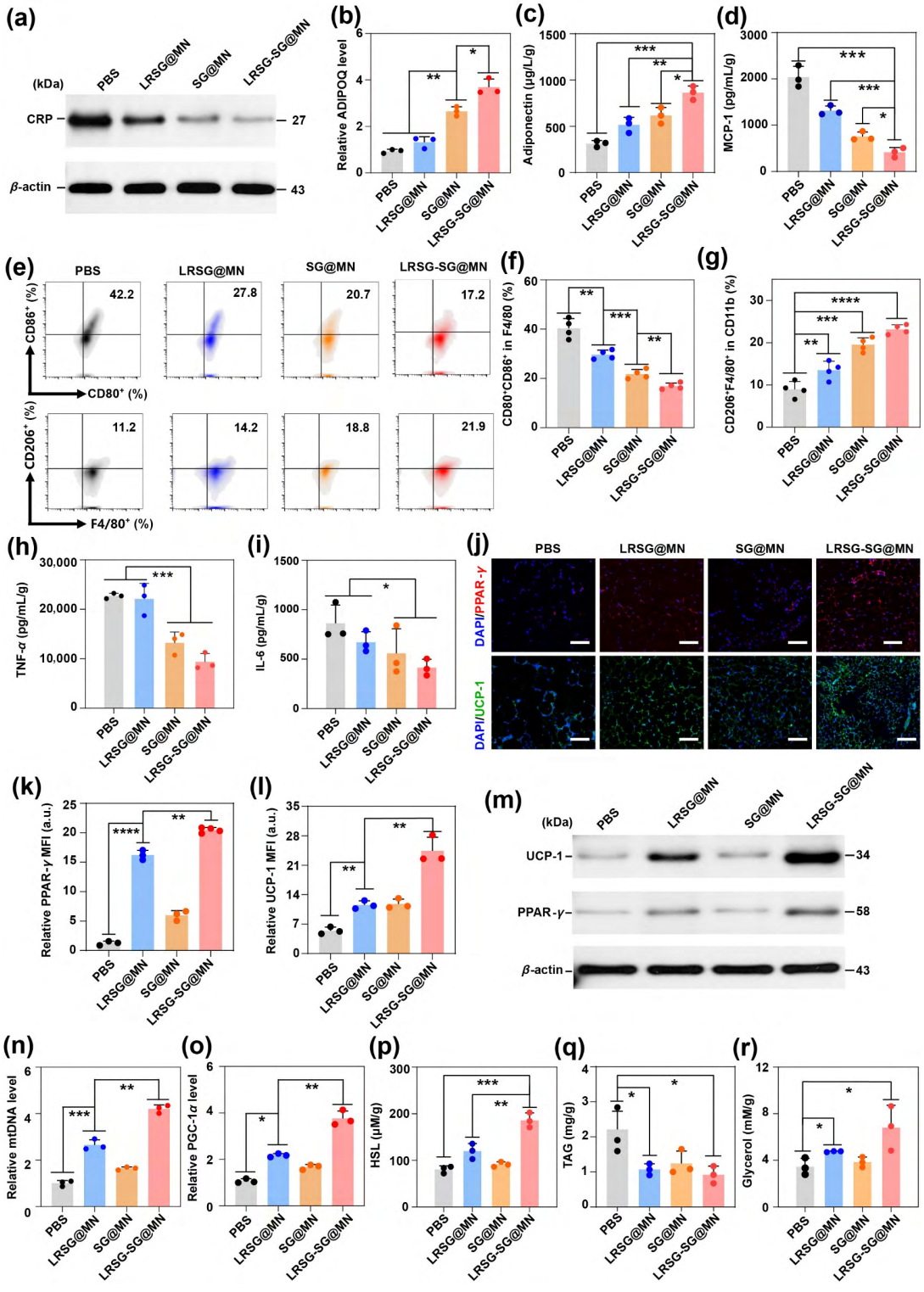

Figure 7 LRSG-SG@MN-mediated synergistic anti-inflammatory and browning anti-obesity effects. (a) Western blot analysis of CRP expression in adipose tissue after different treatments. (b) mRNA expressions of ADIPOQ in adipose tissue (n = 3 biologically independent mice per group). (c) Adiponectin and (d) MCP-1 level in adipose tissue (n = 3 biologically independent mice per group). (e) M1 and M2 phenotypes analysis of macrophage in adipose tissue after different treatments by flow cytometry. The corresponding quantitative results of (f) M1 phenotypes and (g) M2 phenotypes of panel (e) (n = 4 biologically independent mice per group). (h) TNF-α and (i) IL-6 levels in the adipose tissue (n = 3 biologically independent mice per group). (j) Immunofluorescence staining of UCP-1 and PPAR-γ expression in adipose tissue after different treatments. Scale bars: 200 μm. The corresponding quantitative results of (k) PPAR-γ and (l) UCP-1 of panel (j) (n = 3 biologically independent mice per group). (m) Western blot analysis of UCP-1 and PPAR-γ expression in adipose tissue after different treatments. Expressions of (n) mtDNA and (o) PGC-1α in adipose tissue (n = 3 biologically independent mice per group). (p) HSL, (q) TAG, and (r) glycerol level in adipose tissue (n = 3 biologically independent mice per group). Statistical significance was calculated using the one-way ANOVA with Tukey post-hoc analysis. $^*P < 0.05$, $^{**}P < 0.01$, $^{***}P < 0.001$, $^{****}P < 0.0001$. The values are presented as mean ± s.e.m.

90 °C oil bath for 1 h (500 r/min) to obtain the oil phase. The surfactant was slowly added to the vigorously stirred oil phase, thereby generating primary lipid droplets. Subsequently, the primary lipid droplets were subjected to probe sonication in an ice bath (50% power, 2 s on, 3 s off, 5 min) to prepare the final lipid droplets. To evaluate the drug encapsulation efficiency, ultrafiltration centrifugation was used to separate the lipid droplets from free drug. The sample was divided into two fractions (free drug and lipid droplets) via high-speed centrifugation (10,000 rpm, 6 min) using an ultrafiltration tube with a molecular weight cut-off of 300 kDa. RSG in the lipid droplets was then extracted via demulsification with *n*-hexane. The concentrations of RSG in the *n*-hexane solution and the supernatant were determined separately using an ultraviolet–visible (UV–Vis) spectrophotometer. The encapsulation efficiency of RSG in the lipid droplets was calculated using the formula: ((Mass of RSG in lipid droplets)/(Mass of RSG in lipid droplets + Mass of RSG in supernatant)) × 100%. For evaluating the stability of the lipid droplets, the droplets were stored at room temperature for 14 days, and their particle size changes were continuously monitored using a DLS instrument. The morphology of the lipid droplets was observed via TEM.

4.3 Preparation and characterization of LRSG-SG@MN

The polydimethylsiloxane (PDMS) molds for microneedles were purchased from a commercial vendor (Alibaba, Hangzhou, China). The microneedle (fabricated using these molds) had a height of 840 μm, a base diameter of 280 μm, a 15 × 15 array configuration, and an overall mold size of 13.3 mm × 13.3 mm. First, 5 g of starch was dissolved in 95 g of water and stirred to form a suspension, which was then heated in a microwave oven for 1 min to achieve gelatinization. Subsequently, 20% HA, 20% gelatin, and gelatinized starch were mixed at a specific ratio with the volume of gelatinized starch fixed as the reference unit (1 volume equivalent), followed by stirring at 40 °C overnight to prepare the microneedle matrix solution. SG was dissolved in water (pH = 1) to obtain the SG solution. Microneedles were fabricated via the vacuum defoaming method. The lipid droplets, SG solution, and microneedle matrix solution were mixed and stirred for 10 min. Then, 600 μL of the mixed microneedle matrix solution was loaded into the PDMS microneedle molds. Vacuum defoaming was conducted under −0.08 atm for 5 min, and this defoaming process was repeated 3 times. The molds were then placed in an oven at 37 °C for 12 h; after demolding, the microneedles were obtained. The morphology of the microneedles was characterized using an SEM.

4.4 *In vitro* cumulative release assessment

The drug release rate was determined using a UV–Vis spectrophotometer. Microneedles loaded with lipid droplets were placed in the upper chamber of a 6-well Transwell plate, and PBS was added to the lower chamber. At each predetermined time point, all solution in the lower chamber was aspirated and replaced with an equal volume of fresh PBS. The collected samples were dissolved in dimethyl sulfoxide (DMSO), and their absorbance was measured at 312 nm.

4.5 Mechanical analysis

The axial load breaking force of the microneedles was measured using an electronic universal testing machine. Each sample was placed with the microneedle side facing upward, aligned with the sensor. Next, the load cell was moved downward until it contacted the tip of the microneedle. It was then continued to move downward at a speed of 0.5 mm/min, with the displacement and force recorded, until a preset force was reached. Similarly, the toughness of the microneedle material was determined via a tensile test using the same electronic universal testing machine. Samples with a length of 50 mm, width of 14 mm, and thickness of 14.1 mm were fixed, then stretched at a speed of 5 mm/min. The stress and strain were recorded continuously until the samples were completely fractured.

4.6 Skin insertion test

To evaluate the piercing performance of the microneedles, two pieces of porcine skin were naturally thawed. The stratum corneum side of the skin was placed facing upward, and surface moisture was blotted dry with absorbent paper. The microneedles were vertically inserted into the porcine skin; afterward, the skin samples were embedded in paraffin, sectioned, and stained with H&E. For evaluating the transdermal performance of LRSG, microneedles were fabricated by mixing Nile Red-labeled LRSG (10 μg/mL Nile Red, excitation: 528 nm, emission: 576 nm) and fluorescein isothiocyanate (FITC) (10 μg/mL, excitation: 490 nm, emission: 576 nm) into the microneedle matrix solution. The microneedles were vertically inserted into porcine skin and the porcine skin was then embedded in paraffin, sectioned, and fluorescent images were captured using a super-resolution microscope.

4.7 Cell culture

3T3-L1 cells, obtained from the Culture Collection of Wuhan University, were incubated in DMEM supplemented with 10% fetal bovine serum (FBS) and 1% Penicillin-Streptomycin, under an atmosphere of 5% CO_2 at 37 °C. After the cells reached 100% confluency, they were continuously incubated for an additional 48 h to achieve complete contact inhibition. Subsequently, the cells were incubated with differentiation medium (DMEM containing 10% FBS, 1% Penicillin-Streptomycin, 0.5 mM IBMX, 1 μM DXM, and 10 μg/mL insulin) for 48 h. Thereafter, the medium was replaced with adipocyte differentiation medium 2 (DMEM containing 10% FBS, 1% Penicillin-Streptomycin, and 10 μg/mL insulin), and fresh medium was renewed every 48 h until obvious lipid droplets appeared. Finally, the medium was switched to adipocyte maintenance medium (DMEM containing 10% FBS and 1% Penicillin-Streptomycin), with fresh medium replaced every 48 h.

4.8 *In vitro* cell cytotoxicity assay

The MTT (methylthiazolyldiphenyl-tetrazolium bromide) assay was used to evaluate the relative cell viability. Adipocytes that had completed differentiation in a 96-well plate were treated with RSG solutions at different concentrations, followed by continuous incubation for 24 h. Subsequently, a 10% MTT solution was added; after 4 h of incubation, the culture medium in the plate was completely aspirated. Then, 150 μL of DMSO was added to each well, and the plate was gently shaken until the purple crystals were completely dissolved. The absorbance at 570 nm was measured using a microplate reader, and the relative cell viability was calculated. Subsequently, the above-mentioned procedure was also applied to the cytotoxicity assay of SG against RAW264.7 cells.

4.9 Cellular uptake analysis

To evaluate the time-dependent internalization capacity of lipid

droplets by various cell lines (3T3-L1 cells, adipocytes, and HUVECs), cells were pre-seeded in a 24-well plate, with 1 mL of complete DMEM medium added to each well. Lipid droplets labeled with the fluorescent dye DID (25 μg/mL DID) were co-incubated with the cells for different time periods within 24 h. Meanwhile, cell nuclei were stained with Hoechst 33342 (10 μg/mL, 20 min, 37 °C). Fluorescent images were captured at 2, 6, 12, and 24 h using an inverted fluorescence microscope under constant laser intensity. Different fluorescent images of the same visual field were merged using ImageJ software.

4.10 *In vitro* assessment of WAT browning induced by LRSG

3T3-L1 cells were seeded into 12-well plates and induced to differentiate into adipocytes. Subsequently, the cells were co-cultured with PBS, Lipid, RSG, and LRSG for 24 h, respectively. The content of HSL in the supernatant, as well as the contents of glycerol and TAG in the cells, were measured using commercial assay kits. To evaluate the intracellular lipid droplet content, Oil Red O staining was performed. First, 0.7 g of Oil Red O powder was dissolved in 200 mL of 100% isopropanol and stirred overnight to prepare a saturated solution, which was then filtered through a 0.22 μm filter to obtain the Oil Red O stock solution. Next, the Oil Red O stock solution was mixed with deionized water at a volume ratio of 3:2, and the mixture was further filtered through a 0.22 μm filter to prepare the Oil Red O working solution. Cells were fixed with 4% paraformaldehyde solution for 20 min; after fixation, the Oil Red O working solution was added and incubated for 10 min. Following the staining procedure, bright-field images were captured using an inverted fluorescence microscope.

To investigate mitochondrial biogenesis in adipocytes, 3T3-L1 cells were seeded into 12-well plates and induced to differentiate into adipocytes. The cells were then co-cultured with PBS, Lipid, RSG, and LRSG for 24 h, respectively. After these treatments, mitochondria were stained with Mitomarker-Red (5 μg/mL, 10 min, 37 °C), while cell nuclei were stained with Hoechst 33342 (10 μg/mL, 20 min, 37 °C). Fluorescent images were captured using a super-resolution fluorescence microscope under constant laser intensity, and different fluorescent images of the same visual field were merged using ImageJ software. Meanwhile, TEM images of the cells were obtained for morphological observation of mitochondria.

To study the expression of brown adipocyte-specific genes in adipocytes, the treated adipocyte samples were sent to Wuhan Servicebio Technology Co., Ltd. qPCR and Western blotting (WB) were used to detect the expression levels of mtDNA, PGC-1α, UCP-1, and PPAR-γ.

4.11 *In vitro* assessment of anti-inflammatory response induced by SG@MN

RAW264.7 cells were seeded into 12-well plates at a density of 1×10^5 cells per well and incubated overnight. The cells were then stimulated with 100 ng/mL LPS and 20 ng/mL IFN-γ for 24 h to induce M1 polarization. Subsequently, these cells were co-cultured with PBS, MN, SG, and SG@MN for 24 h, respectively. The contents of TNF-α and IL-6 in the supernatant were measured using ELISA kits. To evaluate the anti-inflammatory effect of SG@MN, flow cytometry was used to analyze macrophage polarization. The treated cells were collected, washed with PBS, and resuspended to prepare a cell suspension. For the analysis of M1 macrophages ($F4/80^+CD80^+CD86^+$) and M2 macrophages ($CD11b^+F4/80^+CD206^+$), the cells were stained with corresponding antibodies, including APC-anti-F4/80, PE-anti-CD11b, APC-anti-CD86, FITC-anti-F4/80, PE-anti-CD80, and FITC-anti-CD206. To investigate the effect of SG@MN-regulated macrophage polarization on adipocyte inflammation, the supernatants from macrophages co-cultured with PBS, MN, SG, and SG@MN were subsequently co-cultured with adipocytes in 12-well plates for 24 h. To detect the intracellular ROS levels in adipocytes, the cell-permeable probe DCFH-DA at a concentration of 10 μM was used. The probe was incubated with the cells at 37 °C in the dark for 20 min. After the staining procedure, fluorescent images and bright-field images were captured using an inverted fluorescence microscope, and images of the same visual field were merged using ImageJ software. To investigate the expression of inflammation-related genes in adipocytes, qPCR and WB were used to detect the expression levels of CRP and ADIPOQ.

4.12 Biodistribution of lipid

To assess the retention of lipid droplets *in vivo* and track their *in vivo* distribution, the fluorescent dye Cy5.5 was used. Male C57BL/6J mice (10–12 weeks old) were first fed for 6 weeks. Subsequently, the mice were divided into four groups and administered with Cy5.5, Cy5.5-Lipid, Cy5.5@MN, and Cy5.5-Lipid@MN at the inguinal region, respectively. Fluorescent retention was captured at the same time points on days 1, 2, 3, 4, 5, and 6 using an *in vivo* imaging system (IVIS). Two days after administration, some mice were humanely euthanized, and the biodistribution of Cy5.5-labeled samples in iWAT, eWAT, and pWAT was evaluated.

4.13 Anti-obesity effect of LRSG-SG@MN on HFD-induced obese mice

Male C57BL/6J mice (6 weeks old) were purchased and after 1 week of acclimation, the mice were grouped based on body weight. The mice were fed with HFD (D12492, Research Diets, NJ, USA, 60% kcal fat content) for 60 days. When the body weight of HFD-fed mice exceeded 120% of their baseline body weight, the model was successfully established. The HFD-induced obese mice were randomly divided into 4 groups (n = 4) as follows: HFD-induced obese mice (PBS), obese mice treated with LRSG@MN (RSG content: 5 mg/kg BW), SG@MN (SG content: 1 mg/kg BW), and LRSG-SG@MN (RSG content: 5 mg/kg BW; SG content: 1 mg/kg BW). All treatments were administered once a week and lasted for one month. Body weight and food intake were recorded every three days at the same time.

4.14 *In vivo* anti-obesity effect

After male C57BL/6J mice were fed a high-fat diet for 60 days, PBS, LRSG@MN, SG@MN, and LRSG-SG@MN were administered via microneedles once every week. The body weight of the mice was measured every 3 days. After treatment, GTT, metabolic monitoring, and MRI were performed on the mice. Subsequently, the mice were humanely euthanized. Major organs and tissues were harvested, followed by H&E staining to evaluate organ damage and quantify adipocyte size. Flow cytometry, qPCR, WB, and ELISA kits were used to analyze the anti-inflammatory and adipocyte browning effects. To assess the effect of restoring glucose metabolism in mice, an intraperitoneal glucose tolerance test

(IPGTT) was conducted. Mice were fasted for 16 h with free access to water. Fasting blood glucose was measured using a blood glucose meter, and this measurement time was regarded as the starting time point. Subsequently, glucose (2 g/kg body weight) was administered via intraperitoneal injection, and the blood glucose level of each mouse was measured at 30, 60, 90, and 120 min, respectively. Metabolomics was used to analyze the metabolism of insulin and glucagon in the pancreas. Commercial assay kits were used to determine the contents of TAG, free fatty acids (FFA), and glycerol in adipose tissue.

4.15 ELISA assay

Cell culture supernatants or adipose tissue supernatants were collected after various treatments. For adipose tissue, the samples were weighed immediately after extraction, homogenized, and centrifuged to obtain the supernatants. According to the manufacturer's instructions, ELISA kits were used to measure the concentrations of cytokines (IL-6 and TNF-α).

4.16 Statistical analysis

Statistical analyses were performed using GraphPad Prism 8.4.3 software. Data are presented as mean ± s.e.m. Detailed information regarding statistical tests, P values, and the number of replicates is provided in the figures. A significance threshold of $^{*}P < 0.05$ was used for all experiments, $^{*}P < 0.05$, $^{**}P < 0.01$, $^{***}P < 0.001$, $^{****}P < 0.0001$.

Electronic Supplementary Material: Supplementary material (toughness and elastic modulus of the adipose-targeted nanocomposite microneedle patch (LRSGSG@MN), ROS production and cells cytotoxicity, the biological safety of LRSGSG@MN in obese mice models and the immune analysis) is available in the online version of this article at https://doi.org/10.26599/NR.2026.94908852.

Data availability

All data needed to support the conclusions in the paper are presented in the manuscript and the Electronic Supplementary Material. Additional data related to this paper may be requested from the corresponding author upon request.

Acknowledgements

This work was supported by the National Natural Science Foundation of China (Nos. 52273148, 52333004, and 52473145). The authors would like to acknowledge the Center for Electron Microscopy at Wuhan University for their substantial support for TEM (JEM-2100).

Declaration of competing interest

The authors declare no conflict of interest.

Author contribution statement

W. Q. Y., X. Z., and X. Z. Z.: Conceptualization, project design, formal analysis, methodology, investigation. W. Q. Y. and J. W. W.: Writing – original draft. X. Z., W. H. C., and X. Z. Z.: Conceptualization, investigation, writing – review & editing, resources, funding acquisition, supervision.

Informed consent

Not applicable.

Ethics statement

All the animal experiments were conducted under protocols (AUP, WP20250139) approved by the Institutional Animal Care and Use Committee (IACUC) of the Animal Experiment Center of Wuhan University (Wuhan, P. R. China).

Use of AI statement

None.

References

[1] Larabee, C. M.; Neely, O. C.; Domingos, A. I. Obesity: A neuroimmunometabolic perspective. *Nat. Rev. Endocrinol.* **2020**, *16*, 30–43.

[2] Tilg, H.; Petta, S.; Stefan, N.; Targher, G. Metabolic dysfunction-associated steatotic liver disease in adults: A review. *JAMA* **2026**, *335*, 163–174.

[3] Li, Q.; Hagberg, C. E.; Cascales, H. S.; Lang, S.; Hyvönen, M. T.; Salehzadeh, F.; Chen, P.; Alexandersson, I.; Terezaki, E.; Harms, M. J. et al. Obesity and hyperinsulinemia drive adipocytes to activate a cell cycle program and senesce. *Nat. Med.* **2021**, *27*, 1941–1953.

[4] Bader, J. E.; Wolf, M. M.; Lupica-Tondo, G. L.; Madden, M. Z.; Reinfeld, B. I.; Arner, E. N.; Hathaway, E. S.; Steiner, K. K.; Needle, G. A.; Hatem, Z. et al. Obesity induces PD-1 on macrophages to suppress anti-tumour immunity. *Nature* **2024**, *630*, 968–975.

[5] Coral, D. E.; Smit, F.; Farzaneh, A.; Gieswinkel, A.; Tajes, J. F.; Sparsø, T.; Delfin, C.; Bauvin, P.; Wang, K.; Temprosa, M. et al. Subclassification of obesity for precision prediction of cardiometabolic diseases. *Nat. Med.* **2025**, *31*, 534–543.

[6] Sakers, A.; De Siqueira, M. K.; Seale, P.; Villanueva, C. J. Adipose-tissue plasticity in health and disease. *Cell* **2022**, *185*, 419–446.

[7] Li, Y.; Wang, D. M.; Ping, X. D.; Zhang, Y. K.; Zhang, T.; Wang, L.; Jin, L.; Zhao, W. J.; Guo, M. W.; Shen, F. et al. Local hyperthermia therapy induces browning of white fat and treats obesity. *Cell* **2022**, *185*, 949–966.e19.

[8] Emont, M. P.; Jacobs, C.; Essene, A. L.; Pant, D.; Tenen, D.; Colleluori, G.; Di Vincenzo, A.; Jørgensen, A. M.; Dashti, H.; Stefek, A. et al. A single-cell atlas of human and mouse white adipose tissue. *Nature* **2022**, *603*, 926–933.

[9] Morigny, P.; Boucher, J.; Arner, P.; Langin, D. Lipid and glucose metabolism in white adipocytes: Pathways, dysfunction and therapeutics. *Nat. Rev. Endocrinol.* **2021**, *17*, 276–295.

[10] Maqdasy, S.; Lecoutre, S.; Renzi, G.; Frendo-Cumbo, S.; Rizo-Roca, D.; Moritz, T.; Juvany, M.; Hodek, O.; Gao, H.; Couchet, M. et al. Impaired phosphocreatine metabolism in white adipocytes promotes inflammation. *Nat. Metab.* **2022**, *4*, 190–202.

[11] Lundgren, P.; Sharma, P. V.; Dohnalová, L.; Coleman, K.; Uhr, G. T.; Kircher, S.; Litichevskiy, L.; Bahnsen, K.; Descamps, H. C.; Demetriadou, C. et al. A subpopulation of lipogenic brown adipocytes drives thermogenic memory. *Nat. Metab.* **2023**, *5*, 1691–1705.

[12] Cohen, P.; Kajimura, S. The cellular and functional complexity of thermogenic fat. *Nat. Rev. Mol. Cell Biol.* **2021**, *22*, 393–409.

[13] Harms, M.; Seale, P. Brown and beige fat: Development, function and therapeutic potential. *Nat. Med.* **2013**, *19*, 1252–1263.

[14] Yue, S. J.; Zhai, Z. Z.; An, J. N.; Sun, H. L.; Li, J. Y.; Zhao, C. Z.; Xu, Y.; Zhong, Z. Y. Neutrophil/Leukemia-tropic dual-drug nanomedicine potentiates the treatment of acute myeloid leukemia. *Adv. Mater.* **2026**, *38*, e12635.

[15] Chen, R. H.; Huang, S. S.; Lin, T. T.; Ma, H. S.; Shan, W. J.; Duan,

F.; Lv, J.; Zhang, J. D.; Ren, L.; Nie, L. M. Photoacoustic molecular imaging-escorted adipose photodynamic-browning synergy for fighting obesity with virus-like complexes. *Nat. Nanotechnol.* **2021**, *16*, 455–465.

[16] Zhang, Y. Q.; Liu, Q. M.; Yu, J. C.; Yu, S. J.; Wang, J. Q.; Qiang, L.; Gu, Z. Locally induced adipose tissue browning by microneedle patch for obesity treatment. *ACS Nano* **2017**, *11*, 9223–9230.

[17] Omran, F.; Christian, M. Inflammatory signaling and brown fat activity. *Front. Endocrinol.* **2020**, *11*, 156.

[18] Goto, T.; Naknukool, S.; Yoshitake, R.; Hanafusa, Y.; Tokiwa, S.; Li, Y. J.; Sakamoto, T.; Nitta, T.; Kim, M.; Takahashi, N. et al. Proinflammatory cytokine interleukin-1β suppresses cold-induced thermogenesis in adipocytes. *Cytokine* **2016**, *77*, 107–114.

[19] Sakamoto, T.; Takahashi, N.; Sawaragi, Y.; Naknukool, S.; Yu, R. N.; Goto, T.; Kawada, T. Inflammation induced by RAW macrophages suppresses *UCP1* mRNA induction via ERK activation in 10T1/2 adipocytes. *Am. J. Physiol. Cell Physiol.* **2013**, *304*, C729–C738.

[20] Sakamoto, T.; Nitta, T.; Maruno, K.; Yeh, Y. S.; Kuwata, H.; Tomita, K.; Goto, T.; Takahashi, N.; Kawada, T. Macrophage infiltration into obese adipose tissues suppresses the induction of UCP1 level in mice. *Am. J. Physiol. Endocrinol. Metab.* **2016**, *310*, E676–E687.

[21] Chavakis, T.; Alexaki, V. I.; Ferrante, A. W. Macrophage function in adipose tissue homeostasis and metabolic inflammation. *Nat. Immunol.* **2023**, *24*, 757–766.

[22] Jacks, R. D.; Lumeng, C. N. Macrophage and T cell networks in adipose tissue. *Nat. Rev. Endocrinol.* **2024**, *20*, 50–61.

[23] Yan, J. H.; Hao, P. L.; Zeng, S. M.; Liang, C. X.; Chen, Y.; Chen, K. W.; Qu, W. Q.; Zeng, X.; Zhong, Z. L.; Zhang, X. Z. Injectable multifunctional hydrogels for adipose tissue remodeling to treat obesity and alleviate metabolic syndrome. *J. Controlled Release* **2025**, *381*, 113585.

[24] Drucker, D. J. Mechanisms of action and therapeutic application of glucagon-like peptide-1. *Cell Metab.* **2018**, *27*, 740–756.

[25] Movahednasab, M.; Dianat-Moghadam, H.; Khodadad, S.; Nedaeinia, R.; Safabakhsh, S.; Ferns, G.; Salehi, R. GLP-1-based therapies for type 2 diabetes: From single, dual and triple agonists to endogenous GLP-1 production and L-cell differentiation. *Diabetol. Metab. Syndr.* **2025**, *17*, 60.

[26] Zheng, Z. K.; Zong, Y.; Ma, Y. Y.; Tian, Y. C.; Pang, Y. D.; Zhang, C. Q.; Gao, J. J. Glucagon-like peptide-1 receptor: Mechanisms and advances in therapy. *Signal Transduction Targeted Ther.* **2024**, *9*, 234.

[27] Kim, K. S.; Park, J. S.; Hwang, E.; Park, M. J.; Shin, H. Y.; Lee, Y. H.; Kim, K. M.; Gautron, L.; Godschall, E.; Portillo, B. et al. GLP-1 increases preingestive satiation via hypothalamic circuits in mice and humans. *Science* **2024**, *385*, 438–446.

[28] Wilding, J. P. H.; Batterham, R. L.; Davies, M.; Van Gaal, L. F.; Kandler, K.; Konakli, K.; Lingvay, I.; McGowan, B. M.; Oral, T. K.; Rosenstock, J. et al. Weight regain and cardiometabolic effects after withdrawal of semaglutide: The STEP 1 trial extension. *Diabetes Obes. Metab.* **2022**, *24*, 1553–1564.

[29] Chen, J.; Mei, A. H.; Wei, Y. Y.; Li, C. L.; Qian, H.; Min, X. W.; Yang, H. D.; Dong, L. L.; Rao, X. Q.; Zhong, J. X. GLP-1 receptor agonist as a modulator of innate immunity. *Front. Immunol.* **2022**, *13*, 997578.

[30] Wang, Z. H.; Qing, H. R.; Li, R.; Li, X.; Guo, X.; Zhou, S. B. M2 macrophage-derived exosomes inhibiting neutrophil extracellular traps for ischemic stroke therapy. *Adv. Funct. Mater.* **2024**, *34*, 2402724.

[31] Lu, Y. C.; Luo, Z. Y.; Zhou, H. L.; Shi, Y. Y.; Zhu, Y.; Guo, X. M.; Huang, J. X.; Zhang, J. L.; Liu, X.; Wang, S. J. et al. A nanoemulsion targeting adipose hypertrophy and hyperplasia shows anti-obesity efficiency in female mice. *Nat. Commun.* **2024**, *15*, 72.

[32] You, J. H.; Yang, C. W.; Han, J. P.; Wang, H.; Zhang, W. T.; Zhang, Y.; Lu, Z. Y.; Wang, S. Q.; Cai, R. S.; Li, H. J. et al. Ultrarapid-acting microneedles for immediate delivery of biotherapeutics. *Adv. Mater.* **2023**, *35*, 2304582.

[33] Wang, S. Q.; Yang, C. W.; Zhang, W. T.; Zhao, S.; You, J. H.; Cai, R. S.; Wang, H.; Bao, Y. H.; Zhang, Y.; Zhang, J. et al. Glucose-responsive microneedle patch with high insulin loading capacity for prolonged glycemic control in mice and minipigs. *ACS Nano* **2024**, *18*, 26056–26065.

[34] Guo, J.; Liu, R. H.; Lv, Y. Z.; Xie, H.; Zhou, S. B. Light-encoding of a supramolecular hydrogel for assembly-free soft machines capable of sequential and multistage shape-morphing. *Adv. Funct. Mater.* **2025**, *35*, 2412222.